

Determination of the $E1$ component of the low-energy $^{12}\text{C}(\alpha, \gamma)^{16}\text{O}$ cross section

X. D. Tang,^{1,2} K. E. Rehm,¹ I. Ahmad,¹ C. R. Brune,³ A. Champagne,⁴ J. P. Greene,¹ A. Hecht,¹ D. J. Henderson,¹ R. V. F. Janssens,¹ C. L. Jiang,¹ L. Jisonna,⁵ D. Kahl,^{1,*} E. F. Moore,¹ M. Notani,^{1,†} R. C. Pardo,¹ N. Patel,^{1,6} M. Paul,⁷ G. Savard,¹ J. P. Schiffer,¹ R. E. Segel,⁵ S. Sinha,^{1,‡} and A. H. Wuosmaa⁸

¹Physics Division, Argonne National Laboratory, Argonne, Illinois 60439, USA

²University of Notre Dame, Notre Dame, Indiana 46556, USA

³Ohio University, Athens, Ohio 45701, USA

⁴University of North Carolina, Chapel Hill, North Carolina 27599, USA

⁵Northwestern University, Evanston, Illinois 60208, USA

⁶Colorado School of Mines, Golden, Colorado 80401, USA

⁷Racah Institute of Physics, Hebrew University, Jerusalem, 91904, Israel

⁸Western Michigan University, Kalamazoo, Michigan 49008, USA

(Received 30 December 2009; published 29 April 2010)

A measurement of the β -delayed α decay of ^{16}N using a set of twin ionization chambers is described. Sources were made by implantation, using a ^{16}N beam produced via the In-Flight Technique. The energies and emission angles of the ^{12}C and α particles were measured in coincidence and very clean α spectra, down to energies of 450 keV, were obtained. The structure of the spectra from this experiment is in good agreement with results from previous measurements. An analysis of our data with the same input parameters as used in earlier studies gives $S_{E1}(300) = 86 \pm 22$ keVb for the $E1$ component of the S -factor. This value is in excellent agreement with results obtained from various direct and indirect measurements. In addition, the influence of new measurements including the phase shift data from Tischhauser *et al.* on the value of $S_{E1}(300)$ is discussed.

DOI: 10.1103/PhysRevC.81.045809

PACS number(s): 21.10.Pc, 23.60.+e, 25.55.-e, 26.20.-f

I. INTRODUCTION

The isotopes ^{16}O and ^{12}C are, after ^1H and ^4He , the third- and fourth-most abundant nuclei in the visible universe. Most of the carbon and oxygen which we observe today is produced by helium burning in red giant stars. Carbon and oxygen are not only crucial for all living organisms, but their relative abundances, which are determined by the competition between the triple α and the $^{12}\text{C}(\alpha, \gamma)^{16}\text{O}$ reactions, is also an important parameter for the evolution of a massive star at the end of its lifetime during the carbon-, neon-, and oxygen-burning phases [1–3]. While the cross section for the triple- α process is experimentally quite well determined [4], our knowledge of the $^{12}\text{C}(\alpha, \gamma)^{16}\text{O}$ reaction under typical helium burning conditions [$T_9 \sim 0.2$ or $E_{c.m.} \sim 300$ keV] is still limited by its small cross section and by the crucial role played by two subthreshold states in ^{16}O [5].

The history of experiments studying the $^{12}\text{C}(\alpha, \gamma)^{16}\text{O}$ reaction goes back more than four decades [6,7]. The magnitude of this cross section, however, is still a hotly debated issue, both experimentally and theoretically, and many recent publications can be found in the literature [8–16].

The $^{12}\text{C}(\alpha, \gamma)^{16}\text{O}$ reaction proceeds mainly through two radiative capture modes to the ^{16}O ground state (see Fig. 1). One is $E1$ capture with contributions from the 1^- state at

$E_x = 9.585$ MeV ($E_r = 2.418$ MeV) and the subthreshold 1^- state at $E_x = 7.117$ MeV ($E_r = -45$ keV). The other is $E2$ capture, which is dominated by the contributions from direct capture, and the subthreshold 2^+ state at $E_x = 6.917$ MeV ($E_r = -245$ keV). At energies corresponding to the Gamow window for red giant stars ($E_{c.m.} \sim 300$ keV), the cross sections are of the order of 10^{-17} b. For that reason, all direct measurements so far were done at higher energies above $E_{c.m.} = 890$ keV [4]. These data are then extrapolated into the energy region of astrophysical interest using R -matrix theory. Since the higher-energy data are not very sensitive to the contributions from subthreshold resonances, the published S factors in the past 30 years range from 1 to 288 keVb for $S_{E1}(300)$ and 7 to 120 keVb for $S_{E2}(300)$ [17]. To improve the reliability of the extrapolations, data from complementary experiments, such as elastic α scattering on ^{12}C [18,19], α -transfer reactions to ^{16}O [20], and ^{16}N decay are usually included in the analyses [21].

A measurement of the β -delayed α decay of ^{16}N is considered to be the best method presently available to provide a constrain for the $E1$ component, $S_{E1}(300)$, of the $^{12}\text{C}(\alpha, \gamma)^{16}\text{O}$ reaction [21]. For nuclear astrophysics, this decay has been studied in the past by two groups [11,21–23]. The S -factor $S_{E1}(300)$ is extracted from the relative height of a satellite peak in the α energy spectrum located at $E_\alpha \sim 0.9$ MeV, which originates from the interference of the subthreshold 1^- state with the higher-lying 1^- state in ^{16}O at $E_x = 9.585$ MeV [24].

In all previous experiments [11,21–23,25] the α particles were detected in thin Si surface-barrier detectors. The very small α/β ratio of the ^{16}N decay ($\sim 10^{-5}$), however, results in a very high background from β particles that strongly affects the low-energy part of the energy spectrum from which $S_{E1}(300)$

*Present address: Center for Nuclear Study (CNS), the University of Tokyo, Japan.

†Present address: University of Notre Dame, Notre Dame, Indiana, USA.

‡Present address: University of California, Davis, California, USA.

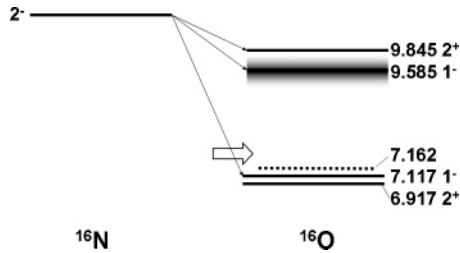


FIG. 1. Spins and excitation energies of excited states in ^{16}O which are relevant for the radiative capture reaction $^{12}\text{C}(\alpha, \gamma)^{16}\text{O}$. The dotted line represents the (α, γ) threshold in ^{16}O (at $E_x = 7.162$ MeV), while the arrow indicates the location of the Gamow window.

is extracted. To alleviate this problem very thin Si detectors (10–15 μm) were used in those experiments. These detectors, however, are not always very homogeneous. Furthermore, Si detectors have dead layers that can affect the energy calibration and they are prone to deterioration, especially during long exposures to radiation.

In the experiment described in this article, we have used a somewhat different approach for measuring the ^{16}N decay. To produce the ^{16}N activity, we used the In-Flight Technique [26], eliminating the $^{17,18}\text{N}$ contamination, which was present in one of the earlier experiments [21,22]. In order to reduce the sensitivity to β particles, we have developed an array of high-acceptance ionization chambers of minimal thicknesses, to be used for the detection of ^{12}C and α particles in coincidence.

A subset of the present data has been published previously [27]. In this article, we give a detailed description of the experimental setup and present an analysis of the full data set. The beam-production method, the detection system and the technique used for stopping the ^{16}N beam is described in Sec. II. A description of the ionization chambers for the coincident detection of ^{12}C - α pairs, their sensitivity to β particles, and a discussion of the backgrounds is given in Sec. III. The experimental results are presented in Sec. IV followed by the R -matrix analysis in Sec. V.

II. SCHEMATIC OF THE EXPERIMENT

A. Production of the ^{16}N beam

The ^{16}N beam was produced by bombarding a deuterium-filled ($p = 1.4$ bar) gas cell [26], which was cooled by liquid nitrogen to temperatures of -180°C , with a 82-MeV beam of ^{15}N . The fully stripped $^{16}\text{N}^{7+}$ ions generated through the inverse kinematics $d(^{15}\text{N}, ^{16}\text{N})p$ reaction were focused with a superconducting solenoid, located immediately behind the production cell, and were subsequently separated from the primary ^{15}N beam by a 22° bending magnet. A superconducting debunching resonator reduced the energy width of the secondary beam by a factor of about two to provide a beam energy of 61.3 ± 0.15 MeV. The beam purity was determined in a separate experiment by measuring mass and Z in the focal plane of a split-pole magnetic spectrograph. Fig. 2 provides a two-dimensional plot of particle range vs. the square of the energy indicating the beam purity (80%) and the

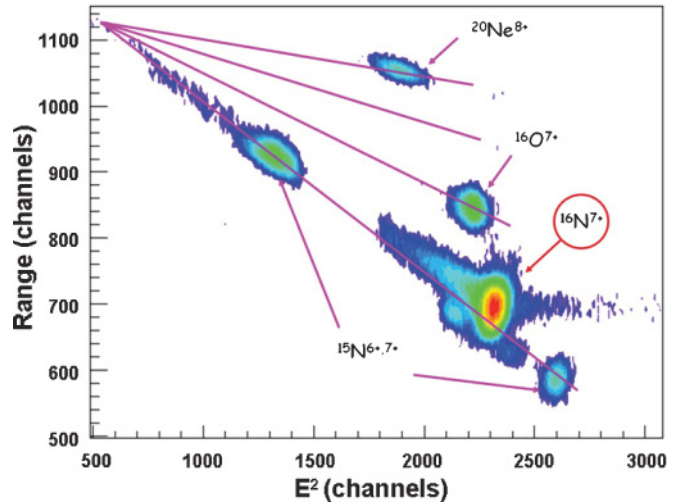


FIG. 2. (Color online) Plot of the particle identification spectrum measured in the focal plane of the split-pole magnetic spectrograph for a secondary ^{16}N beam produced via the In-Flight Technique. The solid lines indicate the predicted locations for various ions. See Ref. [28] for details.

observed contaminants. Details of the identification scheme can be found in Ref. [28]. All of the beam contaminants, ^{15}N from the primary beam, ^{16}O from the $d(^{15}\text{N}, ^{16}\text{O})n$ reaction, and ^{20}Ne from a small primary beam contaminant, are stable isotopes. With a typical current of 100 pA of ^{15}N , secondary ^{16}N beam intensities up to 3×10^6 particles/s were obtained.

B. Detection system

A schematic of the experimental setup can be found in Fig. 3. The ~ 60 -MeV ^{16}N ($t_{1/2} = 7.1$ s) beam was transported by the magnetic elements of the beam line to a gas-filled energy degrader cell located ~ 15 -m downstream from the production target, where the ions were slowed and thereafter stopped in a thin ($17 \mu\text{g}/\text{cm}^2$) carbon foil (foil I), mounted on a rotating wheel located in the main part of the detector chamber (see lower part of Fig. 3). The wheel, which was biased to -350 V also served as cathode to the twin ionization chambers. The degrader cell and the main chamber were filled with P10 counting gas at a typical pressure of 150 Torr. After an irradiation period of 15 s, the beam was stopped for 100 ms and the foil was rotated counterclockwise (in 60 ms) by 120° so that it was located between a pair (pair A) of twin ionization chambers for the coincident detection of α and ^{12}C particles. The carbon foil was counted in this pair of ionization chambers for 15 s. During this time, a second foil (foil II), mounted 120° with respect to the first foil, collected ^{16}N ions. At the end of this collection period, foil II was rotated clockwise to a second pair of ionization chambers (pair B) and counted, while foil I was again collecting ^{16}N ions. Detector-pair A was meanwhile counting a non-irradiated foil (labeled “background foil” in Fig. 3), providing information about the background of the setup during the whole experiment. The same foil was also used for measuring the background in detector-pair B.

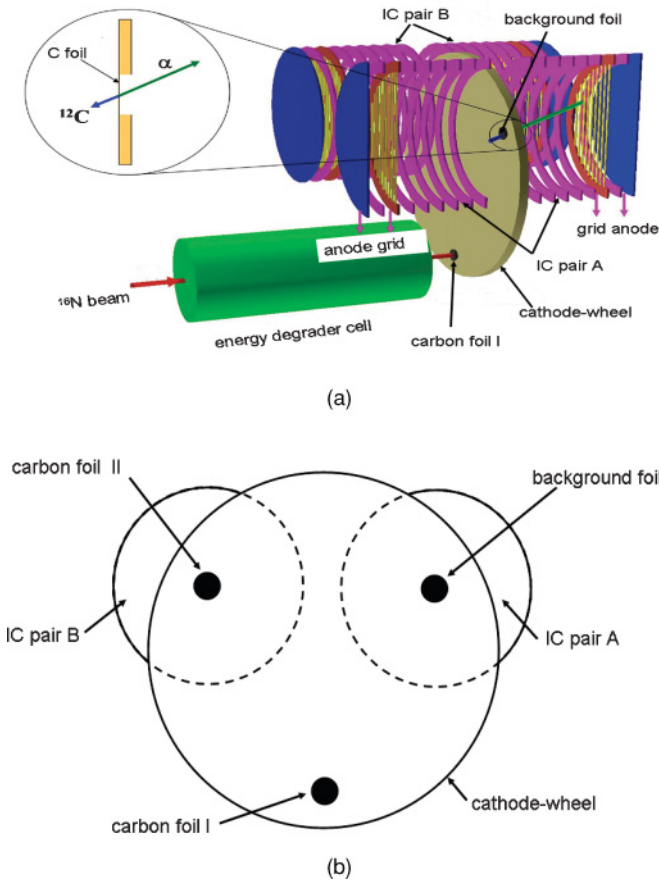


FIG. 3. (Color online) Schematic of the experimental setup used for the measurement of the β -delayed α decay of ^{16}N .

The wheel was rotated by a stepping motor coupled to an encoder with a resolution of $0.01^\circ/\text{step}$. The need to detect particles with very low energies (~ 100 keV) forced us to remove all possible sources of electronic interference. The main noise contribution originated from the holding current of the stepping motor. In order to eliminate this interference, a mechanical brake was installed, which was activated once the wheel was in its proper position. With this brake the stepping motor could be switched off completely during the counting period. A photograph of the entire setup is presented in Fig. 4.

C. Stopping the ^{16}N beam

For the α decay to occur at rest, the ^{16}N particles need to be stopped in a thin carbon-catcher foil. The ~ 60 -MeV ^{16}N ions were first slowed down in the 16-cm long degrader cell filled with P10 gas, with $1.3\text{-mg}/\text{cm}^2$ thick Ti foils as entrance and exit windows (see Fig. 3). An additional $6.75\text{-mg}/\text{cm}^2$ thick Al absorber, installed after the attenuation cell, reduced the energy of the ^{16}N ions to about 250 keV. The gas pressure in the attenuation cell could be adjusted independent of the pressure in the ionization chamber volume in order to maximize the number of ^{16}N particles stopped in the carbon-catcher foils.

In order to test the collection efficiency, several thin foils, including C, Ti, Al, TiN, and melamine with nominal

thicknesses ranging from 10 to $50\ \mu\text{g}/\text{cm}^2$ were mounted on the wheel. A Si detector located at 180° relative to the irradiation position was used to detect the β particles from the ^{16}N decay. The foil was rotated from the irradiation position to the Si detector and the β activity was measured as a function of the gas pressure in the attenuation chamber. The collection efficiency was found to be independent of the chemical composition of the foil.

The thickness of the carbon-catcher foils used in the experiment (nominally $10\ \mu\text{g}/\text{cm}^2$ [29]) was determined to be $17 \pm 2\ \mu\text{g}/\text{cm}^2$ by measuring the energy loss of α particles from a ^{228}Th source in the split-pole magnetic spectrograph.

For a $17\text{-}\mu\text{g}/\text{cm}^2$ C foil, the maximum capture efficiency is about 6% (see Fig. 5). With a $50\text{-}\mu\text{g}/\text{cm}^2$ C foil an efficiency of 20% has been obtained. The energy loss of the recoiling ^{12}C ions, however, would have been too large for such a thick foil. The low capture efficiency of the ^{16}N particles in the carbon foil can be understood from the formation of neutral, ^{16}N -containing molecules that are not attracted by the negatively charged cathode wheel.

D. Possible beam contaminants

Since the count rates in the critical interference region in the present experiment were of the order of a few counts/h, the production of other possible α emitters, in particular $^{17,18}\text{N}$, needs to be considered. The α branching ratios of $^{17,18}\text{N}$ are 2.5×10^{-5} [30] and 0.12 [31], respectively. The small α -decay branch makes ^{17}N a less-important background. For this reason, possible production mechanisms for ^{18}N are discussed first.

The isotope ^{18}N has two peaks in its α spectrum at energies of 1.081 and 1.409 MeV that fall in the energy region which is studied in this experiment. In Refs. [32,33], it has been argued that the α spectrum obtained in our experiment shows contributions from the decay of ^{18}N . While ^{18}N cannot be produced from reactions of ^{15}N with the deuterium in the gas cell, multiparticle transfer reactions on the HAVAR and Ti foils [e.g., $^{48}\text{Ti}(^{15}\text{N},^{18}\text{N})^{45}\text{Ti}$] need to be considered as well. At energies of ~ 5 MeV/u these reactions have “bell-shaped” distributions with their highest yields at $\theta \sim 30^\circ$ [34]. Within the angular acceptance of the beam-transport system around 0° , the cross sections are only hundreds of $\mu\text{b}/\text{sr}$. This translates into production rates of tens of ions/s at the production target. However, due to the negative Q values of these multiparticle transfer reactions ($Q \sim -20$ MeV), the ^{18}N particles could not pass through the beam-transport system. The same holds for fusion-evaporation reactions between ^{15}N and carbon or other light elements suggested in Ref. [33]. Since the Q values of these reactions are very negative [e.g., $Q = -42$ MeV for the reaction $^{12}\text{C}(^{15}\text{N},^{18}\text{N})^9\text{C}$], the reaction is either energetically forbidden, as for the case of ^{12}C , or results in very low-energy $^{17,18}\text{N}$ particles that cannot pass through the beam-transport system after the production target.

These arguments do not apply to ^{18}N particles generated by the ~ 60 -MeV $^{15,16}\text{N}$ beams incident on the Ti entrance foil or the CH_4 gas of the attenuation cell. The ground-state Q value of the $^{48}\text{Ti}(^{16}\text{N},^{18}\text{N})^{46}\text{Ti}$ reaction is about -12 MeV.

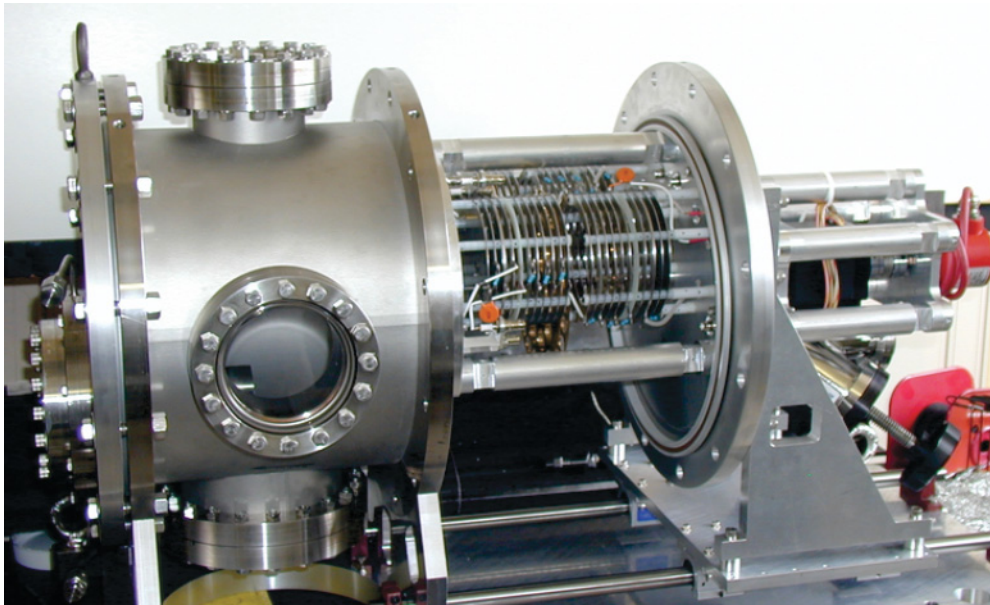


FIG. 4. (Color online) Photograph of experimental setup.

Since no experimental data exist for this reaction, the cross sections of the $^{48}\text{Ca}(^{16}\text{O},^{18}\text{O})^{46}\text{Ca}$ reaction [35] was taken for a rate estimate, resulting in a ^{18}N production rate of ~ 1 ion/h. However, because of the negative Q values (-12 MeV for the ^{16}N -induced reaction or -23 MeV for the ^{15}N -induced reaction), the ^{18}N particles produced in this way will be stopped in the 6.75-mg/cm^2 thick Al absorber located after the attenuation cell and, thus, cannot reach the carbon-stopper foils. Those ^{18}N particles that may be produced by fusion reactions on ^{12}C or ^{16}O contaminants again have very low energies and will not reach the carbon-catcher foils.

Reactions induced by $^{15,16}\text{N}$ on odd- A target contaminants (e.g., ^{13}C , ^{17}O , . . .) have also been considered. These reactions have positive Q values, which could lead to the production of ^{17}N and contribute to the counts in the energy region $E_\alpha = 1\text{--}1.5$ MeV. For an estimate of this component of the ^{17}N -production rate, we assumed that the $^{13}\text{C}(^{16}\text{N},^{17}\text{N})^{12}\text{C}$

reaction ($Q = +0.94$ MeV) was occurring on the ^{13}C ions in the CH_4 component of the P10 gas in the degrader cell. As an estimate, we took a cross section of 10 mb/sr [36] measured for the $^{13}\text{C}(^{16}\text{O},^{17}\text{O})^{12}\text{C}$ reaction. With a beam intensity of 3×10^6 $^{16}\text{N}/\text{s}$ and taking the geometry of the experiment as well as the abundance of ^{13}C in P10 into account, we calculate a ^{17}N -production rate of 0.5 counts/h. The small α/β ratio for ^{17}N (2.5×10^{-5}) [30] and the $\sim 6\%$ stopping efficiency makes this a negligible contribution to the α spectrum.

III. THE TWIN IONIZATION CHAMBERS

A. General description

The main difference between the earlier ^{16}N -decay studies and this experiment is the use of ionization chambers instead of silicon surface-barrier detectors. Compared to silicon detectors, ionization chambers have several advantages for the measurement of α particles from ^{16}N :

- (i) β particles, which for ^{16}N are about 10^5 times more abundant than α particles, experience a very small energy loss in the counting volume (~ 3 keV in this experiment).
- (ii) Ionization chambers are very homogenous and can be tuned to the required thicknesses.
- (iii) They have very high ($\sim 4\pi$) acceptances.
- (iv) They have no dead layers.
- (v) They do not experience radiation damage and are very stable during long experiments.

For our measurement of the α spectrum from the decay of ^{16}N , we have built two pairs of gridded ionization chambers [37,38] for the detection of α - ^{12}C coincidences (see Figs. 3 and 4). Ionization chambers of this type have been used extensively for studies of fission reactions [37], where the

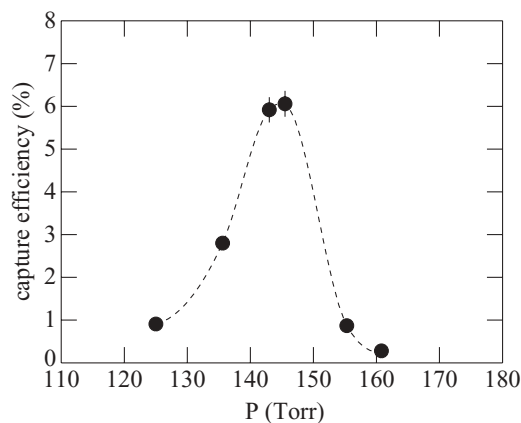


FIG. 5. Capture efficiency of ^{16}N ions in a $17\text{-}\mu\text{g/cm}^2$ thick carbon foil as a function of the pressure in the degrader cell (see text for details).

signals are a factor of 100 higher. The four cylindrical ion chambers (diameter 10 cm, depth 6.5 cm) share a common cathode, which also acts as the target wheel. The voltage of the cathode ($U_{\text{cathode}} = -350$ V) was supplied to the rotating target wheel through a sliding contact. Field-shaping rings (see Figs. 3 and 4) around the active volume provided the required field homogeneity in the active volume. The anode ($U_{\text{anode}} = +200$ V) consists of a 2.5- μm thick aluminized Mylar foil, while the Frisch grid ($U_{\text{fg}} = 0$ V) was produced by soldering 20- μm thick Au-plated tungsten wires to an annular stainless steel frame. The spacing between the wires was 1 mm.

The ionization chambers provide the standard energy signals from the anodes and, from the Frisch grid, information about the angle of emission with respect to the plane of the cathode [37]. The signals from the anode were amplified with Canberra 2003 preamplifiers [39] whereas, for the grid signal, the higher gain eV-550 preamplifiers [40] were used. All signals were then sent to Ortec 572 main amplifiers [41] with 3- μs shaping time for the anode and 0.5 μs for the grid.

Compared to Ref. [37], we have simplified the method for obtaining the angle signal from the Frisch grid. In Ref. [37], the angle signal is obtained by hardware summing the properly calibrated anode and grid signals. In this experiment, we only use the positive lobe of the grid signal, whose height is proportional to the distance of the centroid of the charge distribution from the Frisch grid. While the anode signal provides the total energy of the charged particle, the angle information is obtained from the grid signal G via [37]

$$G \sim E \left[1 - \frac{\langle X \rangle \cos(\theta)}{d} \right], \quad (1)$$

where E is the energy of the particle, $\langle X \rangle$ is the distance from the origin of the emitted particle to the centroid of the charge distribution generated by the particle in the cathode-Frisch grid volume, d is the distance between cathode and Frisch grid, and θ is the angle of the emitted particle with respect to the normal of the cathode plane [37].

B. Calibration and background studies

The ionization chambers were tested and calibrated with standard α sources (^{228}Th and ^{148}Gd) and also with the $^{10}\text{B}(n,\alpha)^7\text{Li}$ and $^6\text{Li}(n,\alpha)t$ reactions using neutrons from a PuBe source, utilizing the α - ^7Li and α -triton coincidences, respectively. The neutron source had a strength of 2×10^6 n/s and was located outside the ionization chamber. Two ^{10}B - ^6Li foils ($10 \mu\text{g}/\text{cm}^2$ ^{10}B and ^6Li evaporated on both sides of a $17\text{-}\mu\text{g}/\text{cm}^2$ C backing) were mounted on the target wheel (see Fig. 6). The neutrons were thermalized in a 2.5-cm thick layer of high-density polyethylene, located outside the chamber. These two reactions produce α particles with energies of 1.472, 1.776, and 2.056 MeV.

A two-dimensional spectrum of grid vs. anode signals from a PuBe calibration run is given in Fig. 6. The vertical groups of events originate from the (n,α) reactions with the α particles emitted at different angles with respect to the foil. The low-

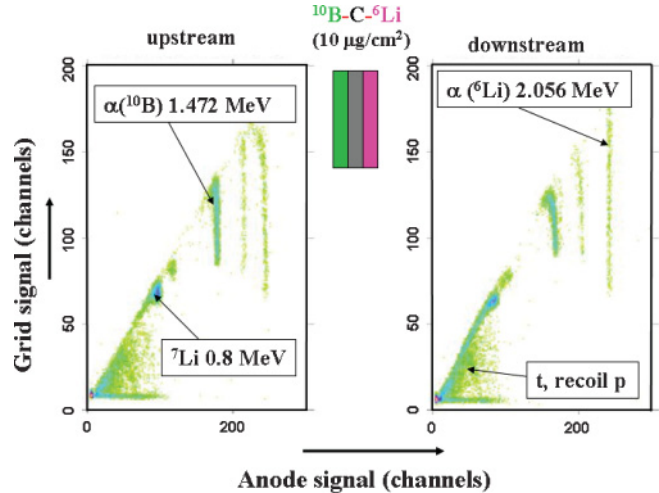


FIG. 6. (Color online) Two-dimensional spectra of grid vs. anode obtained from the twin ionization chamber with a sandwiched target consisting of 10- $\mu\text{g}/\text{cm}^2$ thick layers of ^{10}B and ^6Li evaporated on both sides of a 17- $\mu\text{g}/\text{cm}^2$ carbon foil. The target was bombarded with thermalized neutrons from a PuBe source. The origin of the α particles from ^{10}B or ^6Li are indicated in the figure. The energy-loss effects on the low-energy α particles are visible in the figure (see text for details).

energy events are caused by the coincident ^7Li particles, which have a smaller range in the ion chamber and are all stopped in the vicinity of the target wheel. The α particles emitted perpendicular to the cathode will be stopped closer to the Frisch grid and, therefore, produce a smaller grid signal, while α particles emitted along the foil's surface result in a larger grid signal [see Eq. (1)]. The energy resolution of the four ionization chambers obtained from the 1.472-MeV line is 40 ± 5 keV, which is sufficient to observe the difference (~ 35 keV) in the energies of the α particles after they passed through the C, B, and Li foils and are measured in the upstream or downstream detectors, respectively.

In order to use the calculated α energies one has to be certain that the reaction is, indeed, induced by thermal neutrons. This was confirmed by repeating the measurement with a 1-mm thick Cd foil behind the polyethylene moderator. This reduced the α - ^7Li coincidence rate by more than a factor of 15, in good agreement with estimates.

The $^{10}\text{B}(n,\alpha)^7\text{Li}$ reaction was also used to check the long-term stability of the detectors during the experiment. Over a period of 10 days the stability was found to be better than 3×10^{-3} .

C. Simulation of the detector response

For a measurement of low-energy α - ^{12}C coincidences, three effects need to be carefully investigated:

- (i) The α particles with energies down to at least 0.6 MeV have to be detected in coincidence with 0.2-MeV ^{12}C ions. Any significant energy loss of the outgoing particles in the absorber foil will deform the shape of the spectrum. It is, therefore, crucial to minimize the energy

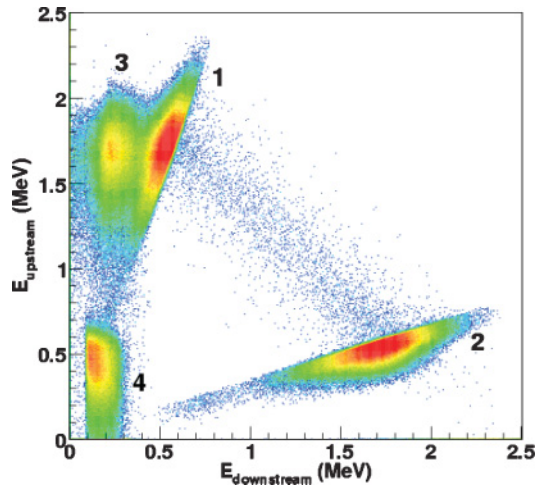


FIG. 7. (Color online) Monte Carlo simulation of the detector response to alpha and ^{12}C particles from the α decay of ^{16}N taking the geometry of the twin ionization chamber into account. The ^{16}N spectrum was taken from Ref. [21].

loss and to reduce the electronic noise so that even the low-energy ^{12}C particles can be clearly identified.

- (ii) If a particle emitted from the foil is stopped in the foil frame, only part of the energy is deposited in the gas. Such an event must be clearly separated from the true coincidences.
- (iii) The detection efficiency must be constant over the important α -energy range from 0.4 to 3 MeV.

A Monte Carlo simulation program was developed to investigate these effects. In the simulations, the theoretical α spectrum from Ref. [21] was used to sample the decay. This spectrum consists of a main peak originating from α particles from the decay of the 1^- state in ^{16}O at $E_x = 9.585$ MeV ($E_\alpha = 1.8$ MeV) and a weaker interference peak at $E_\alpha \sim 0.9$ MeV. An example of such a simulation is presented in Fig. 7. In this calculation, the ionization chamber was filled with P10 gas at a pressure of 150 Torr and the thickness of the catcher foil was $15 \mu\text{g}/\text{cm}^2$. The two main groups, labeled 1 and 2, correspond to α - ^{12}C coincidences identified in the upstream-downstream detectors (1) or downstream-upstream detectors (2), respectively. For these two groups the full energy of both, α particles and ^{12}C ions is deposited in the gas of the ion chamber. This is not the case for the two other groups, labeled (3) and (4), which originate from the asymmetry of the target frame (see Fig. 3). This asymmetry can lead to events where only part of the energy is deposited in the ion chamber before the particle is stopped in the target frame (see Fig. 3). The third group (3), located close to the ordinate, originates from ^{12}C ions that are emitted downstream, but are stopped in the target frame with the full α energy detected in the opposite (upstream) detector. Events in group (4), located in the vicinity of the origin, result from α particles that are emitted downstream, hit the target wheel, and deposit only part of their energy in the P10 gas. It is these events that can overlap with the low-energy α particles from the interference peak.

Events originating from α particles stopped in the target frame (group 4) can easily be separated using their low-energy signals. For events where the ^{12}C ions are stopped in the frame (group 3) an additional angle cut is required, which is discussed in Sec. III D.

The contamination of the low-energy part of the spectrum from partially stopped α particles can be reduced by lowering the pressure in the ionization chambers. In our experiment, a pressure of 150 Torr was chosen. This reduced the upper-energy limit of region (4) to about 400 keV, but it was insufficient to stop α particles with energies above 1.9 MeV. This pressure was considered to be a good compromise, since the main emphasis of the experiment was to study the low-energy part of the α spectrum. In order to determine the shape of the high-energy part of the spectrum, we have also performed measurements with an ionization-chamber pressure of 195 Torr (see Ref. [27]). The measurements were in good agreement with the results from Monte Carlo simulations.

The background events between the two main peaks in Fig. 7 originate from ^{16}N -containing molecules diffusing into the detector volume and producing a signal in both detectors whose sum corresponds to the decay energy of the 1^- state in ^{16}O . In the simulation an (arbitrary) factor of 1% of the total counts was assumed for these events.

After varying the geometrical parameters, an optimum experimental configuration was determined. For a beam-spot diameter of 5 mm, which was defined by a collimator mounted between the degrader cell and the target wheel, we chose a carbon-catcher foil mounted on a target frame with a thickness of 1.75 mm and a 10-mm diameter hole (see Fig. 3). The results of the simulations also provided us with a better understanding of the energy-angle relation obtained from the Frisch-grid and anode signals of the twin ionization chamber (discussed in the next section) and of the pressure dependence of the ionization chambers.

D. Angle information

The angle information obtained from the Frisch grid can be used to eliminate particles that are stopped in the target wheel and give rise to the asymmetry seen in the spectrum of the upstream vs. downstream detectors shown of Fig. 7. From the theoretical alpha spectrum discussed above, we obtain a Monte Carlo simulation of the Frisch grid (angle) vs. anode (energy) spectrum, which is shown in the top part of Fig. 8. An experimental spectrum of the same quantities is given in the bottom part of Fig. 8 for comparison. The solid lines correspond to curves of constant emission angles of 0° (10° 90° (starting from the lowest curve), calculated from Eq. (1). The angle sensitivity is highest for particles emitted closer to the cathode plane. Particles that are emitted at angles that are too close to the carbon foil can be eliminated using the information provided by the Frisch grid.

E. Coincidence efficiency

Because of the asymmetry of the target wheel [see inset to Fig. 3(a)], only ^{12}C - α pairs emitted in the angular range $\theta = 0^\circ$ - 75° deposit their full energy in the twin ionization

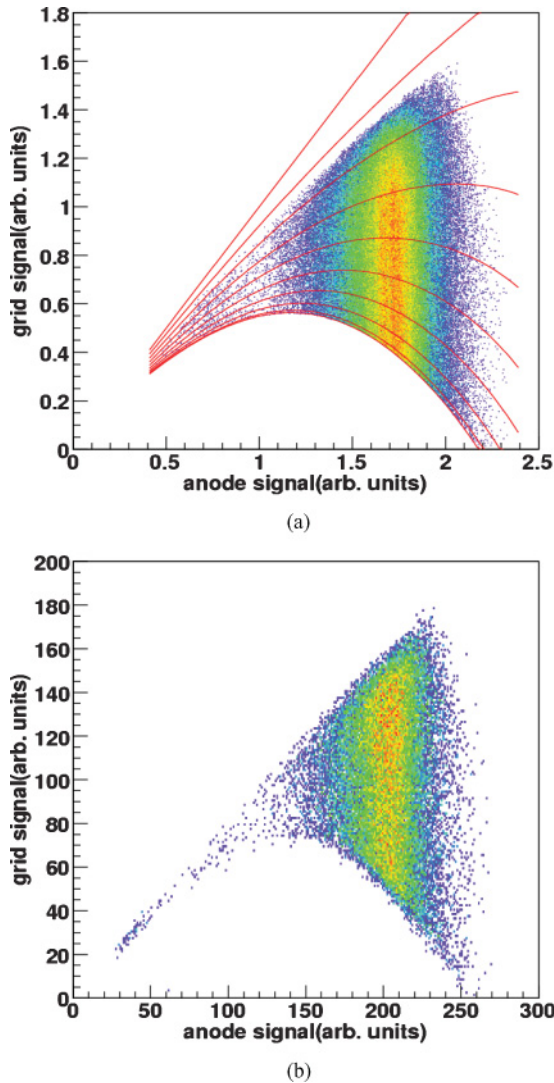


FIG. 8. (Color online) Monte Carlo simulation of the Frisch grid vs. anode spectrum of alpha particles from the α -decay of ^{16}N taking the geometry of the twin ionization chamber into account (top panel). The solid lines correspond to lines of constant emission angles at $\theta = 0^\circ$ (10°) 90° (starting from the bottom), as calculated from Eq. (1). Frisch grid vs. anode spectrum measured with one of the twin ionization chambers in this experiment (bottom panel).

chamber (groups 1 or 2 in Fig. 7). This results in a geometric coincidence efficiency of 75%. For a determination of $S_{E1}(300)$ the energy dependence of the coincidence efficiency is important. The Monte-Carlo simulations mentioned in Sec. III C, which include energy loss and straggling of α particles and ^{12}C ions in the catcher foil, did not indicate any loss in coincidence efficiency down to energies $E_\alpha \sim 300$ -400 keV (corresponding to about 500 keV in the c.m. system). At these energies the coincidences start to overlap with events where the α particle is stopped in the target frame (Fig. 7, group 4).

Since there are no dead layers in the twin ionization chamber the only remaining thresholds come from the electronics. These thresholds were measured by sending pulser signals with the appropriate amplitude ratios to the preamplifiers. This

electronic coincidence efficiency was found to be constant to better than 3% down to c.m. energies of ~ 200 keV in the $^{12}\text{C} + \alpha$ system. These thresholds were further checked through $^{10}\text{B}(n,\alpha)^7\text{Li}$ coincidence measurements with thick ^{10}B targets which provided ^7Li particles down to 400 keV.

F. Background effects

Because of the low count rates expected for the interference peak around $E_\alpha \sim 0.9$ MeV in the α spectrum (typically 3 events/h), the background in the twin ionization chambers needs to be well understood. In addition to beam-related backgrounds, which will be discussed in the following section, the materials used for the construction of the ionization chambers contain natural α emitters that can contribute to the low-energy part of the α spectrum. The insert of Fig. 9 displays a background spectrum of one of the ionization chambers taken at a pressure of 760 Torr. At this pressure, α particles up to about 6 MeV are stopped in the detector volume. The peak at ~ 5.3 MeV is due to α particles from ^{210}Po , which is a well-known source of background in low-count-rate experiments [42]. It is a decay product of ^{210}Pb that is present in the solder used for the construction of the Frisch grid.

The main part of Fig. 9 provides the background spectrum taken at a pressure of 150 Torr and accumulated over a ~ 1 -day period. The total background rate above the threshold of 100 keV was about 150 particles/h.

In order to test the sensitivity of the ionization chambers to an intense flux of β particles, a ^{22}Na β^+ source with a strength of about 10^5 decays/s was mounted on the target wheel. The only change in the spectrum observed with this source was an increase in the background rate below 200 keV

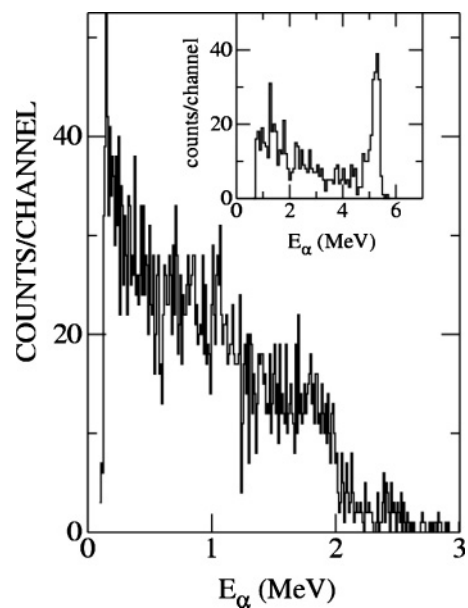


FIG. 9. Background spectrum measured with one of the ionization chambers over a 1-day period at a pressure of 150 Torr. At this pressure only α particles with energies below ~ 2 MeV are stopped within the counting volume. The inset represents a spectrum taken at a pressure of 760 Torr, showing the α line from ^{210}Po at $E = 5.3$ MeV.

of about 60 counts/h. For a ^{12}C - α coincidence measurement, the background induced by β particles is negligible.

The background originating from ^{16}N -containing molecules diffusing from the irradiation region into the ion chambers was minimized by surrounding all ion chambers with a thin layer of Teflon foil.

IV. EXPERIMENTAL RESULTS

The total number of α - ^{12}C coincidences that can be accumulated with this setup is determined by a variety of factors. With an average beam current of 2×10^6 ^{16}N /s, a stopping efficiency of the slowed particles in the $17\text{-}\mu\text{g}/\text{cm}^2$ carbon foil of 6%, a counting efficiency of 0.38, originating from the various irradiation, counting, and rotation times, and a branching ratio for populating the 1^- state at $E_x = 9.585$ of 1×10^{-5} [5], we obtain an α - ^{12}C coincidence rate of the whole array of about 27 counts/m or 4×10^4 /d. Including the time needed for producing the secondary ^{16}N beam, for setting up the electronics, and for the $^{10}\text{B}(n,\alpha)^7\text{Li}$ measurements and other calibrations performed at regular intervals throughout the run, about 4×10^5 coincidences were accumulated in two one-week-long runs.

A two-dimensional ^{12}C - α coincidence spectrum of one detector pair taken at a pressure of 150 Torr is presented in the top panel of Fig. 10 with the corresponding background spectrum shown in the lower panel. The structure observed in the coincidence spectrum is very close to the one obtained in the simulation calculation shown in Fig. 7. The effects of the asymmetry of the target, which influences the α and ^{12}C particle pairs emitted at angles close to the carbon foil are clearly visible. The two main islands correspond to the α - ^{12}C coincidences emitted into the two different detectors. The background observed in the lower panel of Fig. 10 near the origin is beam related and originates from proton recoils generated in the P10 counting gas by neutrons generated downstream of the ^{16}N production target, where the intense primary ^{15}N beam is stopped.

Various combinations of the four parameters E_α , $E_{^{12}\text{C}}$, θ_α and $\theta_{^{12}\text{C}}$ can be used to eliminate the remaining background contributions. As an example, Fig. 11 provides a spectrum of the ratio of pulse heights measured in the downstream and upstream detectors, $E_\alpha/E_{^{12}\text{C}}$ vs. $E_{\text{c.m.}}$, for events located in a triangular-shaped window that selects coincidence pairs from group 2 in Fig. 10. The c.m. energies in Fig. 11 and 12 were obtained by multiplying the α energy by the factor $[M(^{12}\text{C}) + M(^4\text{He})]/M(^{12}\text{C})$. As was done in Ref. [21], the fact that the ^{16}N decay events must have an energy ratio of 3:1 provides a restriction for data selection. Since pulse-height defects in gas counters are smaller than for Si detectors, the pulse-height ratio is on average about 3.4, closer to the theoretical value of 3.0; for the Si detectors used in Ref. [21] this ratio was 4.2.

The asymmetry in the coincidence spectra in Fig. 10 required an additional condition for selecting the α spectra from group 1 (see Fig. 7). The data presented in Ref. [27] were taken from coincidence spectra by selecting events with the α particle emitted downstream (i.e., events of group 2 in Fig. 7). The events had to be within the allowed region of Frisch grid

vs. anode signals (as shown in Fig. 8) for both α particles and ^{12}C particles and had to have a pulse height ratio $E_\alpha/E_{^{12}\text{C}} \geq 3$. In addition a low-energy cut of 450 keV in the energy of the α particles was applied.

For events where the α particle is emitted downstream (i.e., events of group 1 in Fig. 7) an additional angle cut in the Frisch-grid-anode spectrum along the $\theta = 70^\circ$ line [see Fig. 8(a)] was applied, eliminating events with angles $\theta \geq 70^\circ$. Because of the additional software cut, the statistical uncertainties for this spectrum were increased by a (conservative) factor of 1.5.

The total number of counts for the two groups, which were accumulated during two one-week-long runs, is about 345 000. The counts N_1 and N_2 from the two spectra were then combined giving a lower weight to the data which require an additional software condition via the equation:

$$N = N_1 + \frac{N_2}{1.5^2}. \quad (2)$$

The statistical uncertainty is taken as $N^{1/2}$. The α spectrum for these events is shown in Fig. 12, plotted as function of $E_{\text{c.m.}}$, and the data are tabulated in Table I.

As mentioned in Sec. IV C, α particles with energies above $E_\alpha \sim 1.9$ MeV are not stopped in the ionization chamber operating at a pressure of 150 Torr. For that reason the data at higher energies were modified with correction factors obtained

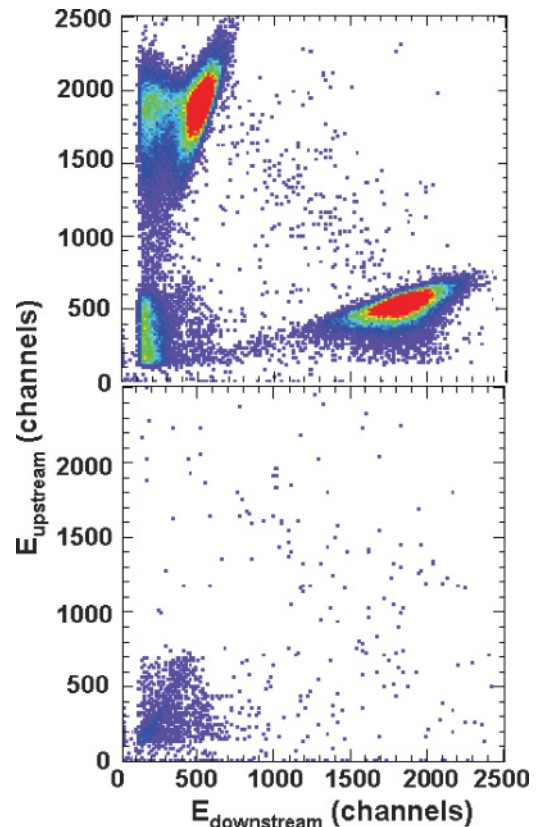


FIG. 10. (Color online) Coincidence spectrum measured with one of the twin ionization chambers for one of the foils implanted with ^{16}N particles (top panel). The lower panel shows the same spectrum, but for a non-implanted foil, measured during the same time and under the same conditions (see text for details).

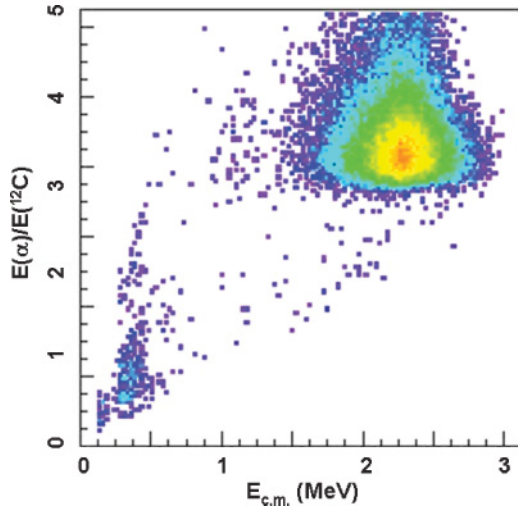


FIG. 11. (Color online) Spectrum of pulse height ratio $E_\alpha/E_{^{12}\text{C}}$ vs. α energy for α - ^{12}C coincidences from one ionization-chamber pair. From momentum conservation, the events should have a pulse-height ratio of 3. Pulse-height defects in the ion chamber and energy losses in the carbon foil lead to slightly larger values. The events close to the origin are caused by recoil protons generated in the P10 gas through neutrons from the production target.

from an independent measurement at 195 Torr [27] and the uncertainties for all events with α energies above 1.9 MeV were increased by 50%.

The α spectrum in Fig. 12 has the same overall shape as the ones measured in the previous experiments [11,21–23]. The main peak is due to the population of the 1^- resonance at $E_x = 9.585$ MeV decaying via the $^{12}\text{C} + \alpha$ channel. The shoulder around $E_{c.m.} = 1.1$ MeV is the interference peak between the 9.585 MeV and the sub-threshold 7.117 MeV 1^- states. The height of this interference peak is proportional to

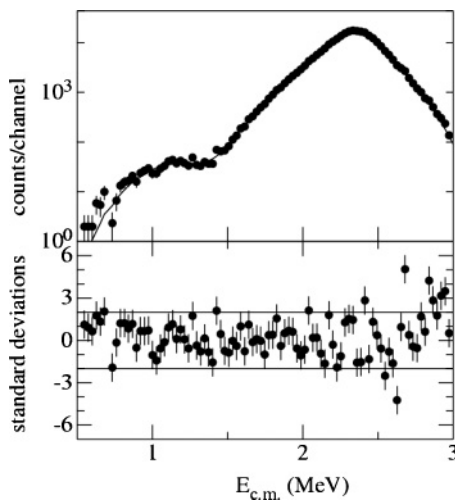


FIG. 12. Spectrum of α particles from the decay of ^{16}N (plotted as function of $E_{c.m.}$), as obtained in this experiment (top). The solid line is the result of an R -matrix least-squares fit, which is discussed in Sec. V A. The bottom plot shows the deviations of the data from the fitted values in units of standard deviations.

TABLE I. α spectra obtained in this experiment. N and Δ are the counts and uncertainties of the α - ^{12}C pairs. The number of counts are rounded to the nearest integer. The least-squares fits discussed below were done with the nonrounded data.

E_α keV	N counts	Δ	E_α keV	N counts	Δ	E_α keV	N counts	Δ
450	2	1	1090	65	8	1710	15416	124
470	6	2	1110	68	8	1730	16706	129
490	5	2	1130	83	9	1750	17466	132
510	10	3	1150	112	11	1770	17182	131
550	2	2	1170	135	12	1790	16596	129
570	7	3	1190	188	14	1810	15934	126
590	13	4	1210	206	14	1830	13774	117
610	16	4	1230	288	17	1850	12230	111
630	17	4	1250	330	18	1870	10276	101
650	21	5	1270	410	20	1890	8472	92
670	16	4	1290	498	22	1910	6804	124
690	24	5	1310	583	24	1930	5658	113
710	27	5	1330	744	27	1950	4527	101
730	30	5	1350	896	30	1970	3492	89
750	23	5	1370	1111	33	1990	3062	83
770	24	5	1390	1251	35	2010	2673	78
790	29	5	1410	1526	39	2030	1944	66
810	33	6	1430	1816	43	2050	1515	58
830	41	6	1450	2143	46	2070	1193	52
850	44	7	1470	2471	50	2090	1007	48
870	37	6	1490	2891	54	2110	761	41
890	42	6	1510	3434	59	2130	687	39
910	38	6	1530	4225	65	2150	505	34
930	34	6	1550	4821	69	2170	367	29
950	49	7	1570	5665	75	2190	304	26
970	35	6	1590	6555	81	2210	235	23
990	33	6	1610	7624	87	2230	136	18
1010	40	6	1630	9240	96	2250	102	15
1030	37	6	1650	10493	102	2270	69	12
1050	37	6	1670	11895	109	2290	10	5
1070	70	8	1690	13596	117	2310	11	5

$S_{E1}(300)$. The solid line is the result of an R -matrix calculation discussed in the following section.

The lower part of Fig. 12 gives the deviations of the various data points from the R -matrix fit normalized to standard deviations. The largest deviations (~ 5 standard deviations) are observed around $E_{c.m.} = 2.68$ MeV, which corresponds to the excitation energy of a narrow ($\Gamma = 0.62$ keV) 2^+ state in ^{16}O at $E_x = 9.68$ MeV. The data points in this energy region were not included in the least-squares fits mentioned below.

It has been argued [33] that the deviation around $E_{c.m.} = 1.4$ MeV (which is at the 2σ level) might have its origin in an ^{18}N beam contaminant. ^{18}N has an α line corresponding to an energy of $E_{c.m.} = 1.390$ MeV. As pointed out in Sec. II D, the probability of having ^{18}N particles transmitted to the catcher foil is negligible. We have also investigated the time distribution of the events in this energy region. The sum of all α particles from the decay of ^{16}N ions after they are implanted in the carbon foil follows an exponential decay with a half-life of 7.5 ± 0.4 s, which is in agreement with the known half-life of ^{16}N (7.1 s). The events in the vicinity of $E_{c.m.} = 1.4$ MeV

are not consistent with the 0.63-s half-life of ^{18}N , but show a half-life of 8.7 ± 3.8 s, again consistent with ^{16}N decay.

V. R-MATRIX ANALYSIS

The analysis of the data has been performed within the R -matrix formalism [43]. The determination of $S_{E1}(300)$ is usually done by a simultaneous fit to data of the direct measurement of the $^{12}\text{C}(\alpha, \gamma)^{16}\text{O}$ reaction performed at higher energies, combined with the results from the delayed α spectrum from ^{16}N , and phase-shift data from elastic scattering of α particles on ^{12}C . In this article, we adopted the same procedure for the least-square fits as done in Ref. [21]. In this section, we present only the relevant equations used in the fitting program and refer to Ref. [21] for a more detailed discussion.

The energy dependence of the α spectrum following the β decay of ^{16}N is given by an (incoherent) sum of the $\ell = 1$ and 3 contributions:

$$W_\alpha = f_\beta(E) \sum_{\ell=1,3} P_\ell(E, a_\ell) \times \left| \frac{\sum_{\lambda=1}^{q_\ell} \frac{A_{\lambda\ell}}{E_{\lambda\ell} - E}}{1 - [S_\ell(E, a_\ell) - B_\ell - iP_\ell(E, a_\ell)]R_\ell(E)} \right|^2, \quad (3)$$

where $f_\beta(E)$ is the integrated Fermi function and $P_\ell(E, a_\ell)$ is the penetrability at a given channel radius a_ℓ . $A_{\lambda\ell}$ are the β -feeding amplitudes of each level included in the fit. $S_\ell(E, a_\ell)$ is the shift factor and B_ℓ the boundary parameter, which is chosen to be $B_\ell = S_\ell(E_{1,\ell}, a_\ell)$. With this choice $E_{1,\ell}$ becomes the energy of the subthreshold $\ell = 1, 3$ levels in ^{16}O . The function $R_\ell(E)$ is calculated from

$$R_\ell(E) = \sum_{\lambda=1}^{q_\ell} \frac{\gamma_{\lambda\ell}^2}{E_{\lambda\ell} - E}, \quad (4)$$

with $\gamma_{\lambda\ell}$ being the reduced α widths of the individual levels included in the fit.

The $E1$ component of the radiative capture cross section $^{12}\text{C}(\alpha, \gamma)^{16}\text{O}$ is given by

$$\sigma_{E1}(E) = \frac{6\pi}{k_\alpha^2} P_1 \left| \frac{\sum_{\lambda=1}^{q_1} \frac{\gamma_{\lambda,1} \Gamma_{\lambda\gamma}^{1/2}}{E_{\lambda,1} - E}}{1 - (S_1 - B_1 - iP_1)R_1} \right|^2, \quad (5)$$

where k_α is the wave number of the α particle in the c.m. system and $\Gamma_{\lambda\gamma}$ is the γ -ray width of level λ calculated by

$$\Gamma_{\lambda\gamma} = 2E_\gamma^3 \gamma_{\lambda\gamma}^2. \quad (6)$$

The $\alpha + ^{12}\text{C}$ phase shifts δ_1 and δ_3 are parameterized by:

$$\delta_\ell(E) = -\Phi_\ell + \arctan \left(\frac{P_\ell}{R_\ell^{-1} - S_\ell + B_\ell} \right), \quad (7)$$

where Φ_ℓ is the hard-sphere phase shift calculated at the channel radius a_ℓ .

The fitting program from Ref. [44] was employed, which simplifies the comparison with the earlier data from Ref. [21]. To account for the experimental resolution in our experiment

(40 keV), the theoretical calculations are folded with a Gaussian distribution before computing the corresponding χ^2 value. The R -matrix parameters were adjusted to minimize the total χ^2 , which is the sum of the individual χ^2 values from all data sets included in the fit. The best $S_{E1}(300)$ factor is calculated from the R -matrix parameters, which provide the global minimum χ_{\min}^2 . The statistical uncertainty for $S_{E1}(300)$ is estimated by accepting those fits with $\chi^2 \leq \chi_{\min}^2 \times (1 + 9/\nu)$, where ν is the number of degrees of freedom (see Ref. [21] and Sec. V B). The systematic uncertainties are derived by varying the quantity under investigation within a reasonable range about its best-fit or best-known value.

A. R-matrix fits with standard input parameters

The α spectrum measured in this experiment covers the c.m. energy range of 0.6 to 3.08 MeV. (The range covered in Ref. [21] was 0.787 to 3.19 MeV).

For the $E1$ radiative capture process, contributions were included from the subthreshold 1^- state at $E_x = 7.117$ MeV, the 1^- state at $E_x = 9.585$ MeV, and a higher lying, otherwise unknown, background 1^- state, which represents the tails of other higher-lying 1^- states. It was shown earlier [21] that including only p wave contributions results in an unrealistically deep minimum in the ^{16}N α spectrum at 1.2 MeV. For this reason, an additional f -wave component with contributions from three 3^- states ($E_x = 6.13, 11.601$ MeV, and an additional background state) is included in the calculations.

Several data sets of the $^{12}\text{C}(\alpha, \gamma)^{16}\text{O}$ reaction have been reported in the literature [8,9,17,45–49]. Of these, only the later measurements of Refs. [8,9,17,45,47–49] have separated out the $E1$ component from the total capture cross sections. In the R -matrix analysis of Ref. [21], only data from Refs. [45,47–49] were used. Recently, two new direct measurements of $S_{E1}(300)$ were carried out [8,9,17] covering the c.m. energy range of 0.89 to 2.8 MeV. In order to simplify the comparison with earlier results, we will, in this section, only use the combined data set from the direct measurements of Refs. [45,47–49]. The influence of the new data on $S_{E1}(300)$ will be discussed in the following section.

For the $\alpha + ^{12}\text{C}$ phase shifts, again several data sets are available [15,18,19,50,51]. In the analysis of Ref. [21] only the data from Plaga *et al.*, [18] were used. The measurements from Refs. [50,51] were discarded because they require significant adjustments of the energy scale. Elastic scattering of $^{12}\text{C}(\alpha, \alpha)^{12}\text{C}$ was remeasured at the University of Notre Dame to provide accurate phase-shift data in the c.m. energy range of 2.6 to 8.2 MeV [15,19]. In this section, we will analyze the data using the phase shifts from Ref. [18]. The influence of the new phase shifts is discussed in the following section.

Some of the parameters were kept fixed during the fit, in order to reduce the number of free variables. These parameters include the energy and γ width of the 1^- level at $E_x = 7.117$ MeV ($E_{\text{c.m.}} = -0.0451$ MeV, $\Gamma_\gamma = 55 \pm 3$ meV), the energy of the 3^- level at $E_x = 6.130$ MeV ($E_{\text{c.m.}} = -1.032$ MeV, taken from Ref. [5]), the β branching ratio of the subthreshold 1^- state $Y_b(7.117) = 4.8 \pm 0.4\%$ (again taken from Ref. [5]). The influence of a recent

measurement [52] for $Y_b(7.117)$ giving a slightly larger value and a smaller uncertainty ($5.2 \pm 0.2\%$) is discussed in the following section. Altogether there are 14 free parameters in the fit (9 associated with the p -wave and 5 with the f -wave contribution).

To verify the performance of the R -matrix code, we repeated the analysis of Ref. [21] using their input data. The best channel radius was determined by searching for the minimum χ^2_{\min} in a plot of channel radius vs. $S_{E1}(300)$ factor. The global minimum was found at a channel radius $a = 6.5$ fm, with $S_{E1}(300) = 78 \pm 15$ keVb, in good agreement with the results of Ref. [21] [$S_{E1}(300) = 79 \pm 16$ keVb]. Following the same procedure and replacing the TRIUMF data with the results from this experiment, the least squares fits were repeated. In this case, the minimum occurs at a channel radius $a = 5.5$ fm with $S_{E1}(300) = 86 \pm 20$ keVb. We have also performed least-squares fits to the two individual data sets N_1 and N_2 followed by the calculation of a weighted average of $S_{E1}(300)$. This procedure gave the same results within the experimental uncertainties. A contour plot of χ^2 in the channel radius a vs. $S(E1)$ plane and the $S(E1)$ dependence of χ^2 on the various components used in the least squares fit are provided in Fig. 13. We find a rather weak (≤ 4 keVb) dependence

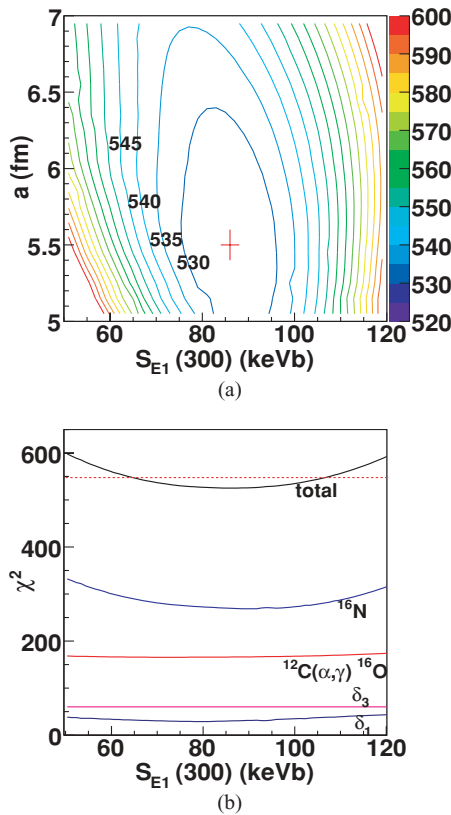


FIG. 13. (Color online) Contour plot of the χ^2 values from the least-squares fit in the channel radius a vs. $S(E1)$ plane (top panel). The lowest contour line corresponds to a value of $\chi^2 = 530$, with an increase of 5 units for the subsequent lines. The minimum χ^2 occurs for a channel radius $a = 5.5$ fm and $S_{E1}(300) = 86$ keVb. Variation of the χ^2 values as function of $S_{E1}(300)$ at a channel radius $a = 5.5$ fm (bottom panel). See text for details.

TABLE II. Parameters obtained from the R -matrix fits. Parameters in parentheses are kept fixed during the fit. Values in brackets are calculated from a fixed input and one fitted parameter ($\gamma_{1,\ell}$).

Parameter	This work	This work	Ref. [21]
Channel radius a (fm)	5.5	6.5	6.5
E_{11} (MeV)	(-0.0451)	(-0.0451)	(-0.0451)
γ_{11} (MeV $^{1/2}$)	0.1771	0.0788	0.0793
$\gamma_{1\gamma}$ (MeV $^{-1}$) $\times 10^6$	[8.819]	[8.756]	[8.761]
$A_{11}/\sqrt{N_\alpha}$ (MeV $^{1/2}$)	[0.216]	[0.0956]	[0.0947]
E_{21} (MeV)	3.3332	2.866	2.845
γ_{21} (MeV $^{1/2}$)	0.5133	0.332	0.330
$\gamma_{2\gamma}$ (MeV $^{-1}$) $\times 10^6$	-1.6713	-2.44	-2.439
$A_{21}/\sqrt{N_\alpha}$ (MeV $^{1/2}$)	0.376	0.185	0.184
E_{31} (MeV)	18.57	11.89	11.71
γ_{31} (MeV $^{1/2}$)	1.6539	1.065	1.017
$\gamma_{3\gamma}$ (MeV $^{-1}$) $\times 10^6$	-5.747	-2.823	-2.819
$A_{31}/\sqrt{N_\alpha}$ (MeV $^{1/2}$)	-0.763	-0.611	-0.640
E_{13} (MeV)	(-1.032)	(-1.032)	(-1.032)
γ_{13} (MeV $^{1/2}$)	0.202	0.1011	0.0765
$A_{13}/\sqrt{N_\alpha}$ (MeV $^{1/2}$)	[0.508]	[0.253]	[0.192]
E_{23} (MeV)	5.252	4.799	4.798
γ_{23} (MeV $^{1/2}$)	0.3457	0.252	0.251
$A_{23}/\sqrt{N_\alpha}$ (MeV $^{1/2}$)	0	0	0
E_{33} (MeV)	168	19.38	17.71
γ_{33} (MeV $^{1/2}$)	5.136	1.318	1.244
$A_{33}/\sqrt{N_\alpha}$ (MeV $^{1/2}$)	0	0	0
$S_{E1}(300)$ (keVb)	86 ± 20	82 ± 25	79 ± 16
χ^2/ν	2.49	2.52	1.76

of $S_{E1}(300)$ on the channel radius for radii between 5.5 and 6.5 fm, consistent with the results of Ref. [21]. It is clear that the ^{16}N data provide the most sensitive constraint on the $S_{E1}(300)$ factor. The results of the least-squares fits for the channel radii of 5.5 fm and 6.5 fm are summarized in Table II and compared with the parameters obtained in Ref. [21]. The solid line in Fig. 12 is also obtained from these calculations.

B. Systematic uncertainties

The uncertainties quoted in Table II are statistical only. For the systematic error budget, three major sources have been identified in Ref. [21]. The largest contribution in their analysis originated from the energy calibration of the Si detectors which contributes ± 10 keVb to the systematic uncertainty. The twin ionization chambers used in this experiment were regularly calibrated with three α lines from slow-neutron induced (n, α) reactions on ^{10}B and ^6Li and the linearity of the electronics was checked with pulse generators. This reduced the contribution from the energy calibration to the systematic uncertainty to ± 5 keVb. The second-largest contribution to the systematic uncertainty comes from the β -decay branching ratio between the subthreshold 1^- state ($E_x = 7.117$ MeV) and the higher lying 1^- state ($E_x = 9.585$ MeV). For this, we have remeasured the branching ratio to the subthreshold 1^- state [52]. The result is 10% higher than the value from Ref. [5] with an uncertainty of about 2%. With this new branching ratio, the optimum $S_{E1}(300)$ factor decreases to

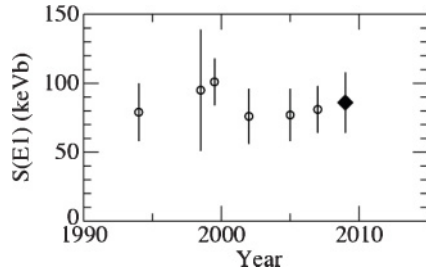


FIG. 14. $S_{E1}(300)$ values taken from the literature published during the last 15 years (open circles). The value from this experiment is shown by the solid diamond. Numerical values are given in Table III.

81 keVb (at $a = 5.5$ fm) and the contribution to the systematic uncertainty term is reduced to ± 2 keVb. The third-largest term in Ref. [21] was attributed to the ^{17}N contamination. Since, as pointed out earlier, we had a negligible contamination from ^{17}N , this term disappears in our experiment. The uncertainty of the radiative width of the subthreshold 1^- state gives an additional contribution of ± 2 keVb. The use of the four sets of independent $^{12}\text{C}(\alpha, \gamma)^{16}\text{O}$ measurements used in the fitting procedure [45,47–49] introduces ± 4 keVb to the systematic uncertainty, while a $\pm 10\%$ uncertainty in the overall normalization of the $^{12}\text{C}(\alpha, \gamma)^{16}\text{O}$ cross section data contributes ± 2 keVb. Adding up all contributions in quadrature, the total systematic uncertainty of our result is ± 8 (sys) keVb.

Adding to the value for $S_{E1}(300)$ in Table II (86 ± 20 keV) the systematic uncertainty of 8 keVb discussed above, we obtain from this experiment a value of $S_{E1}(300) = 86 \pm 20(\text{stat}) \pm 8$ (sys) keVb. Adding both contributions in quadrature gives $S_{E1}(300) = 86 \pm 22$ keVb.

The $S_{E1}(300)$ value of 86 ± 22 keVb obtained in this experiment agrees within the uncertainties with data obtained during the last 15 years, which are summarized in Fig. 14 and in numerical form in Table III together with the $S_{E2}(300)$ values, if available. Since the data entering the various analyses shown in Fig. 14 are not independent, they cannot be averaged.

TABLE III. $S(E1)$ and $S(E2)$ values obtained by various experiments performed since 1994.

$S(E1)$ keVb	$S(E2)$ keVb	Ref.
86 ± 22		This work
	53 ± 16	[19]
79 ± 21		[21]
95 ± 44		[55]
101 ± 17	42 ± 20	[20]
76 ± 20	85 ± 30	[17]
77 ± 19	80 ± 25	[8]
81 ± 17		[10]
74 ± 21		[27]

C. Sensitivity of $S(E1)$ to other input data

In the last few years several new measurements of parameters used in the least-squares fits have been carried out. Two new direct measurements of the $^{12}\text{C}(\alpha, \gamma)^{16}\text{O}$ reaction have been published [9,17,53]; the branching ratio of the subthreshold 1^- state has been re-measured [52] with higher accuracy and new phase shifts of $\alpha + ^{12}\text{C}$ scattering have become available [15,19]. As discussed above, the impact of the 10% higher branching ratio is a decrease of the value $S_{E1}(300)$ by about 5 keVb, which is small compared to the other uncertainties.

After replacing the combined set of the direct measurements [45,47–49] with the new (α, γ) data, the fitting procedure was repeated, keeping the remaining parameters at the same values as before. For the data set of Ref. [21], the minimum χ^2/ν (1.12) occurred at a channel radius $a = 6.5$ fm with $S_{E1}(300) = 83 \pm 12$ keVb. Using the data from this experiment, the minimum ($\chi^2/\nu = 2.0$) occurs at a channel radius $a = 5.5$ fm with $S_{E1}(300) = 90 \pm 20$ keVb. Again these results indicate that the influence of the new direct measurements on $S_{E1}(300)$ is relatively small (~ 4 keVb).

As shown in Ref. [33], the use of the phase shift data of Ref. [18] for obtaining reliable values of $S_{E1}(300)$ has limitations. This conclusion was confirmed in the analysis mentioned above by the appearance of systematic deviations from the experimental data. To investigate the impact of different phase-shift data [15,19], we have used the new phase shifts for p - and f -wave scattering, together with the available ^{16}N β -delayed α -decay spectra and the combined data set of direct $^{12}\text{C}(\alpha, \gamma)^{16}\text{O}$ measurements. In order to eliminate contributions from higher-lying states, the energy range of the p -wave phase shifts was limited to $E_{c.m.} = 0\text{--}4$ MeV. The results of the least-squares fits are summarized in Table IV.

Replacing the phase shifts from Ref. [18] with the new data from Ref. [15] reduces $S_{E1}(300)$ to 53 keVb ($\chi^2/\nu = 0.74$) (using the ^{16}N data from [21]) or to 71 keVb ($\chi^2/\nu = 1$) (using the present data). This large change in $S_{E1}(300)$ indicates that there is a tension between the β -delayed α spectra and the new phase-shift data [15], since both try to constrain the parameters of the 1^- resonance at $E_x = 9.585$ MeV ($E_{c.m.} = 2.42$ MeV). One possible origin, which is mentioned in Ref. [15], might be a difference in the energy calibrations between the two experiments. To illustrate this, a fit to the $^{12}\text{C}(\alpha, \gamma)^{16}\text{O}$ data [45,47–49], the ^{16}N data from Ref. [21], and

TABLE IV. Results of least squares fits using different phase shifts and ^{16}N data. The channel radius used was 6.5 fm for the data from Ref. [21] and 5.5 fm for the present data. The error quoted is the statistical uncertainty only. Using the phase shifts from Ref. [15] (see second line), the energy shifts in E_α of the ^{16}N data are -5 keV for Ref. [21] and -3.75 keV for this experiment, respectively. See text for details.

Ref. for ^{16}N data	Ref. [21]		This work	
	$S_{E1}(300)$ keVb	χ^2/ν	$S_{E1}(300)$ keVb	χ^2/ν
Phase shifts [18]	78 ± 15	1.8	86 ± 20	2.5
Phase shifts [15]	76 ± 10	0.42	85 ± 15	0.95

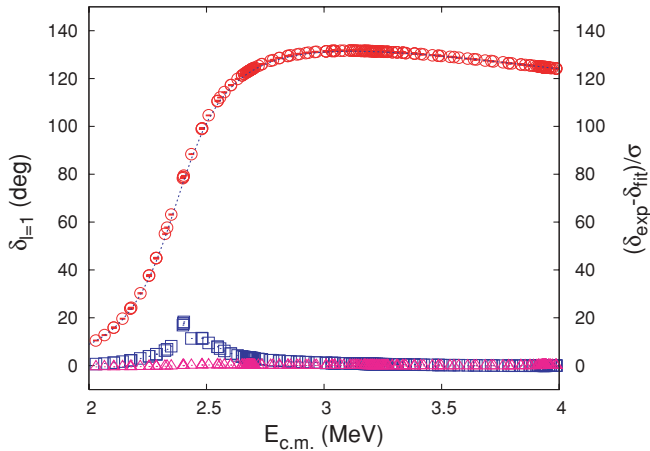


FIG. 15. (Color online) Comparison between the phase shift data for $l = 1$ from Ref. [15] (red circles) and the prediction from a least-squares fit to the $^{12}\text{C}(\alpha, \gamma)^{16}\text{O}$ data [45,47–49], the ^{16}N results from Ref. [21], and the f -wave ($l = 3$) phase-shift data [15] (dotted line). The channel radius used in the calculations was 6.5 fm [19]. The blue squares represent the deviations between the two sets, normalized to the respective uncertainties $(\delta_{\text{exp}} - \delta_{\text{cal}})/\sigma$. For the triangles, the ^{16}N data have been shifted by $E_{\alpha} = -5$ keV. See text for details.

the f -wave ($l = 3$) phase shift data [15] has been performed. The predicted p -wave ($l = 1$) phase shifts based on this fit are shown in Fig. 15 by the dotted line together with the measured p -wave data from Ref. [15] (open circles). The relative uncertainties $(\delta_{\text{exp}} - \delta_{\text{cal}})/\sigma$ (open squares) are also included. The deviations in the vicinity of the 1^{-} state at $E_{\text{c.m.}} = 2.42$ MeV suggest a difference in the energy calibration between the two experiments. By allowing a -5 keV shift in the α energy of the ^{16}N data [21], the deviations can be eliminated, as shown by the triangles in Fig. 15. The values for $S_{E1}(300)$ are 76 keVb using the data from Ref. [21] and 85 keVb for the data from this experiment (see Table IV). The issues regarding this energy shift as well as the treatment of the statistical and systematic uncertainties in Ref. [15] need to be investigated in more detail in the future.

If we combine our data of the ^{16}N decay with the most recent measurements of the direct $^{12}\text{C}(\alpha, \gamma)^{16}\text{O}$ reaction [9,17,53] and the new value for the branching ratio to the subthreshold 1^{-} state [52], but still keeping the phase-shift data from Ref. [18], we obtain a final value of

$$S_{E1}(300 \text{ keV}) = 84 \pm 19(\text{stat}) \pm 8(\text{sys}) \text{ keVb},$$

which by adding both contributions in quadrature gives

$$S_{E1}(300 \text{ keV}) = 84 \pm 21 \text{ keVb}.$$

VI. SUMMARY

A new measurement of the β -delayed α spectrum has been performed. The experiment uses a set of high-efficiency, gas-filled twin ionization chambers, which are practically insensitive to the high β background experienced in these experiments. This allowed us to measure the α spectrum to very low energies without interference from the tail of the β spectrum. We have practically eliminated contributions from $^{17,18}\text{N}$ particles. R -matrix fits have been performed to the α spectra including earlier results of $^{12}\text{C} + \alpha$ phase shifts, capture cross sections, and β branching ratios. Including the statistical uncertainty as well as an 8-keVb systematic uncertainty, the S factor for $E1$ capture extrapolated to the critical energy region $E_{\text{c.m.}} \sim 300$ keV was found to be $S_{E1}(300 \text{ keV}) = 86 \pm 22$ keVb. Least-squares fits including the latest results for β branching ratios and direct $^{12}\text{C}(\alpha, \gamma)^{16}\text{O}$ measurements give $S_{E1}(300 \text{ keV}) = 84 \pm 21$ keVb.

The experiment described in this paper measures only the $E1$ contribution to the astrophysical S factor. For the total S factor, the $E2$ part and contributions from cascade transitions have to be added. While for the $E1$ component the recent data of $S_{E1}(300)$ seem to converge, the S_{E2} data still exhibit large fluctuations. Data published within the last 10 years quote values of 42 ± 20 keVb [20], 53_{-18}^{+13} keVb [19], 85 ± 30 keVb [17], 80 ± 25 keVb [8].

The influence of more recent measurements of the $^{12}\text{C}(\alpha, \gamma)^{16}\text{O}$ reaction and $\alpha + ^{12}\text{C}$ phase shifts on the value of $S_{E1}(300)$ was also investigated. While the new radiative capture experiments show very small effects on the $S_{E1}(300)$ value, there seems to be tension between the new phase shifts and the spectra from the α decay, which needs to be resolved.

ACKNOWLEDGMENTS

We want to thank the crew of the ATLAS accelerator for providing the high-quality ^{15}N beams. The help of B. Nardi and B. Zabransky with the design and construction of the experimental setup is gratefully acknowledged. We are indebted to J. Powell for making a copy of his thesis and his R -matrix code available to us. The help of N. Scielzo with the calculations is also appreciated. One of us (KER) wants to thank M. Mutterer (TU Darmstadt) for explaining the advantages of twin ionization chambers. This work was supported by the US Department of Energy, Office of Nuclear Physics, under Contracts No. DE-AC02-06CH11357 (ANL), DE-FG02-98ER41086 (NWU) and by the NSF Grant No. PHY-02-16783 (Joint Institute for Nuclear Astrophysics).

- [1] T. A. Weaver and S. E. Woosley, *Phys. Rep.* **227**, 65 (1993).
- [2] S. E. Woosley and T. A. Weaver, *Astrophys. J. Suppl.* **101**, 181 (1995).
- [3] G. Wallerstein *et al.*, *Rev. Mod. Phys.* **69**, 995 (1997).
- [4] L. R. Buchmann and C. A. Barnes, *Nucl. Phys.* **777**, 254 (2006).
- [5] www.tunl.duke.edu/nucldata.

- [6] H. M. Loebenstein, D. W. Mingay, H. Winkler, and C. S. Zaidins, *Nucl. Phys. A* **91**, 481 (1967).
- [7] R. J. Jaszczak, J. H. Gibbons, and R. L. Macklin, *Phys. Rev. C* **2**, 63 (1970).
- [8] J. W. Hammer *et al.*, *Nucl. Phys. A* **752**, 514c (2005).
- [9] M. Assuncao *et al.*, *Phys. Rev. C* **73**, 055801 (2006).

- [10] A. Belhout *et al.*, *Nucl. Phys. A* **793**, 178 (2007).
- [11] R. H. France, E. L. Wilds, J. E. McDonald, and M. Gai, *Phys. Rev. C* **75**, 065802 (2007).
- [12] P. Descouvemont, *J. Phys. G* **35**, 014006 (2008).
- [13] C. Matei, C. R. Brune, and T. N. Massey, *Phys. Rev. C* **78**, 065801 (2008).
- [14] F. Strieder, *J. Phys. G* **35**, 014009 (2008).
- [15] P. Tischhauser *et al.*, *Phys. Rev. C* **79**, 055803 (2009).
- [16] H. Makii *et al.*, *Phys. Rev. C* **80**, 065802 (2009).
- [17] R. Kunz *et al.*, *Astrophys. J.* **567**, 643 (2002).
- [18] R. Plaga *et al.*, *Nucl. Phys. A* **465**, 291 (1987).
- [19] P. Tischhauser *et al.*, *Phys. Rev. Lett.* **88**, 072501 (2002).
- [20] C. R. Brune *et al.*, *Phys. Rev. Lett.* **83**, 4025 (1999).
- [21] R. Azuma *et al.*, *Phys. Rev. C* **50**, 1194 (1994).
- [22] L. R. Buchmann *et al.*, *Phys. Rev. Lett.* **70**, 726 (1993).
- [23] Z. Zhao *et al.*, *Phys. Rev. Lett.* **70**, 2066 (1993).
- [24] J. Humblet, *Phys. Rev. C* **42**, 1582 (1990).
- [25] K. Neubeck, H. Schober, and H. Wäffler, *Phys. Rev. C* **10**, 320 (1974).
- [26] B. Harss *et al.*, *Rev. Sci. Instrum.* **71**, 380 (2000).
- [27] X. D. Tang *et al.*, *Phys. Rev. Lett.* **99**, 052502 (2007).
- [28] K. E. Rehm and F. L. H. Wolfs, *Nucl. Instrum. Methods A* **273**, 262 (1988).
- [29] ACF Metals (www.techexpo.com/firms/acf-metl.html).
- [30] M. Dombisky *et al.*, *Phys. Rev. C* **49**, 1867 (1994).
- [31] Z. Zhao *et al.*, *Phys. Rev. C* **39**, 1985 (1989).
- [32] L. Buchmann, *Contribution to the International Conference Nuclei in the Cosmos-X*, (2008).
- [33] L. Buchmann, G. Ruprecht, and C. Ruiz, *Phys. Rev. C* **80**, 045803 (2009).
- [34] L. Pomorski, J. Tys, and V. V. Volkov, *Phys. Lett.* **23**, 369 (1966).
- [35] Y. Eisen *et al.*, *Phys. Rev. C* **13**, 699 (1976).
- [36] P. Debevec, H. J. Körner, and J. P. Schiffer, *Phys. Rev. Lett.* **31**, 171 (1973).
- [37] C. Budtz-Jorgensen *et al.*, *Nucl. Instrum. Methods Phys. Res. A* **258**, 209 (1987).
- [38] A. Göpfert, F. J. Hamsch, and H. Bax, *Nucl. Instrum. Methods Phys. Res. A* **441**, 438 (2000).
- [39] www.canberra.com.
- [40] www.evmicroelectronics.com.
- [41] www.ortec-online.com.
- [42] F. T. Avignone *et al.*, *Phys. Rev. C* **34**, 666 (1986).
- [43] A. M. Lane and R. G. Thomas, *Rev. Mod. Phys.* **30**, 257 (1958).
- [44] J. Powell, Ph.D. Thesis, University of Toronto, 1994.
- [45] P. Dyer and C. A. Barnes, *Nucl. Phys. A* **233**, 495 (1974).
- [46] K. U. Kettner *et al.*, *Z. Phys. A* **308**, 73 (1982).
- [47] A. Redder *et al.*, *Nucl. Phys. A* **462**, 385 (1987).
- [48] R. M. Kremer *et al.*, *Phys. Rev. Lett.* **60**, 1475 (1988).
- [49] J. M. L. Ouellet *et al.*, *Phys. Rev. Lett.* **69**, 1896 (1992).
- [50] C. M. Jones, G. C. Phillips, R. W. Harris, and E. H. Beckner, *Nucl. Phys.* **37**, 1 (1962).
- [51] G. J. Clark, D. J. Sullivan, and P. B. Treacy, *Nucl. Phys. A* **110**, 481 (1968).
- [52] K. E. Rehm *et al.* (Phys. Rev. C to be published).
- [53] R. Kunz *et al.*, *Phys. Rev. Lett.* **86**, 3244 (2001).
- [54] L. Buchmann, R. E. Azuma, C. A. Barnes, J. Humblet, and K. H. Langanke, *Phys. Rev. C* **54**, 393 (1996).
- [55] G. Roters, C. Rolfs, F. Strieder, and H. P. Trautvetter, *Eur. Phys. J. A* **6**, 451 (1999).